Daniel Ellis[1a], Matthew Goodson[1], Michael Miles[2], Troy Munro[1*]

Optimized design for a device to measure thermal contact conductance during Friction Stir Welding

[1]Brigham Young University, Department of Mechanical Engineering, Provo, Utah, USA

[2]Brigham Young University, Department of Manufacturing Engineering, Provo, Utah, USA

[*]troy.munro@byu.edu

ORCID(s): [a]0000-0002-3654-4267

Abstract

Friction stir welding (FSW) is a solid-state welding process that is finding increasing use in a variety of industries, owing to its ability to create high quality welds with less heat input than fusion welding. While the modeling of FSW has been an active effort for at least 15 years, two input parameters, namely the friction coefficient and the heat transfer coefficient, are still adjustable quantities that are difficult to measure. This lack of information compromises the predictive capability of FSW models. While the modeling of friction between the tool and workpiece remains a complex task, the measurement of heat transfer should be possible, but has not be adequately addressed because of the difficulty of accessing the relevant interface with thermocouples. This paper presents a multi-layered frequency-domain thermoreflectance (FDTR) method and transducer design to measure the heat transfer coefficient between the spinning tool and the workpiece. Due to constraints of the welding process, a multi-layered structure is needed for a useable measurement to maximize the heat flow from the modulated heating surface through the heat transfer interface into the welded workpiece. An analytical 2D thermal quadrupole model is shown to be useful in determining layer properties. A multi-layered structure for a specific tool design is validated using COMSOL and optimized. This process can be used to determine the ideal transducer structure to maximize the signal from an FDTR measurement during a friction stir welding process.

Keywords

thermal quadrupoles, FDTR, FSW, heat transfer coefficient

Declarations

Not applicable

Funding

NSF – 1935767

Conflicts of interest/Competing interests

Not applicable

Availability of data and material

Available upon request

Code availability

Available upon request

1. Introduction

1.1 Friction Stir Welding Overview

Friction Stir Welding (FSW) is a solid-state joining process that mechanically joins two metals through a combination of frictional heating and plastic deformation. A non-consumable tool with a pin spins, heats, and compresses the material with sufficient force ($3 - 8.4\ kN$) [1] in a manner that facilitates joining, as shown in Figure 1a. When the temperature of the workpiece is high enough, the tool can translate across the joint and create a high quality bond [2].

FSW has proven to be effective with aluminum alloys in shipbuilding and marine industries, aerospace, automotive and rail industries [3]. Fuel tanks for spacecraft, commercial jets, wheel rims, suspension arms, rail vehicles, and nuclear waste encapsulation have all made use of FSW [3]. In general, FSW has been shown to weld materials, like high strength aluminum, that conventional fusion welding cannot [4], [5]. In particular, the rates of tool rotation [6] and tool translation [7], [8] affect welding temperatures and may give rise to a variety of defects as shown in Figure 1b. These defects weaken the weld [9] and can require significant welding development effort before the process inputs are fully tuned to produce the desired characteristics.

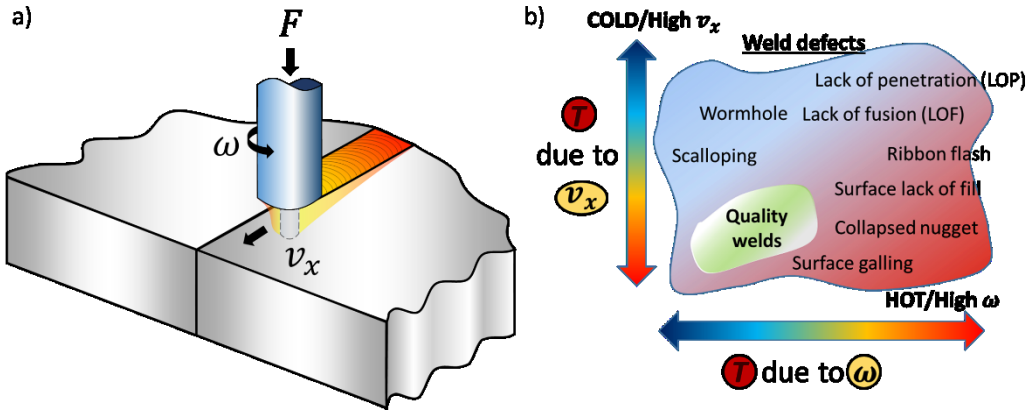

Figure 1. a) Schematic of friction stir welding, with force (F), angular velocity (ω) and translational velocity (v_x) shown. b) Effect of welding process parameters (Including temperature, T) on joint quality, adapted from Arbegast [9].

Accurate simulation models should help to limit this trial and error method of tuning input parameters. However, current FSW models have two critical parameters that have not yet been experimentally measured with enough accuracy to be useful: the friction coefficient (μ), and the heat transfer coefficient between the workpiece and spinning tool surface ($h_{W/T}$) (akin to and used interchangeably with the thermal contact conductance). The heat transfer coefficient between the workpiece and baseplate ($h_{W/B}$) and the heat transfer coefficient between the workpiece and the surrounding air ($h_{W/A}$) are also considered but have less of an impact on the temperature of the weld than $h_{W/T}$. The heat transfer coefficient at the tool/workpiece interface (which is the terminology used in FSW literature) is the inverse of the thermal contact resistance $R = h^{-1}$, and will be referred to as h, in the present paper. The common practice is to tune μ after selecting the various h values based on two often cited papers [10]. The authors specify multiple times that the values obtained, however, are very approximate [11], [12]. Figure 2 shows the current range of h values found in literature for the three interfaces. Note that these values are scattered by two to three orders of magnitude. Some finite

element method (FEM) simulations have shown that using values of $h_{W/B}$ between 500 and $3{,}000\ Wm^{-2}K^{-1}$ can increase both the temperature of the weld and the size of the heat affected zone [13]. That study shows the impact the h values have on predicted weld characteristics and the importance of correct h values for accurate modeling.

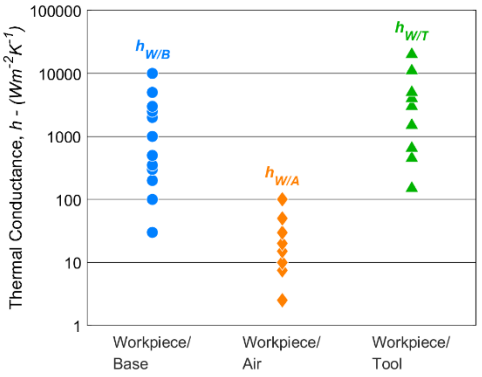

Figure 2. The range of commonly used h values has a two to three orders of magnitude spread, with the least amount of data present for the heat transfer coefficient between the tool and the workpiece, $h_{W/T}$ [10]–[39].

Several papers indicate that approximate values for parameters h and μ were used, because they were too difficult to measure [40], [41]. The ability to measure at least one of these parameters would greatly reduce the tuning needed to achieve more robust model predictions. The current paper presents a method that can be used to directly measure $h_{W/T}$, as well as demonstrating a method to design an appropriate measurement tool that can be used in other measurement configurations.

1.2 Previous Methods to Determine h

Currently, h during FSW is determined by matching thermocouple data taken during FSW tests to the temperature field solved with a FEM model [42]. This common inverse method is done by estimating values for the heat flux and h, keeping μ constant, and adjusting h until the difference between thermocouple data and the FEM model are minimized. This inverse method has had varying levels of success for TIG welding [16] and lathe processes [43], [44]. The drawback with this approach is that heat transfer coefficient needs to be a known quantity at each interface in addition to fixing the friction factor.

Other standard methods of determining h, such as ASTM guarded hot plate methods [45], [46], are dependent on reaching a steady-state and require a significant amount of time [47], [48]. This method has been used to measure h between similar steel materials at pressures expected during FSW [17]. The issue is that steady-state techniques can never be used in real-time during the FSW process because FSW is highly transient. They also cannot characterize the complex thermomechanical environment under the tool, where shearing of the workpiece material is taking place.

Other methods use transient-based approaches, such as the established 3-omega technique [49]–[51], using a high-speed infrared camera [52], the laser-flash method [53], [54], and photo-acoustics [55]. Photothermal techniques [56] are of particular interest to this paper because of their adaptability and ability to probe localized heat transfer. Within the photothermal technique are

thermoreflectance methods such as time-domain thermoreflectance (TDTR) [57] and frequency-domain thermoreflectance (FDTR) techniques [58].

Thermoreflectance methods are based on relating the change in reflectivity of a metal to a change in the temperature of the metal. In TDTR, a thin metal film (transducer) is coated on a bulk material or layered material. Usually with TDTR the time scales are so short, that only nm thin films can be used because the heat does not travel far enough [57]. Attaining a stable nm thin transducer directly in contact at the tool/workpiece interface is not reasonable due to the extreme mechanical and thermal strains found in a typical FSW tool head. Furthermore, TDTR requires complex instrumentation which would be difficult to place in a FSW setup. Instead FDTR will be used for the current research.

Similar to TDTR, FDTR also uses the phenomena of thermoreflectance. A pump beam is incident on a surface that converts the photonic energy into thermal energy. The heat conducts through the material, resulting in a change in temperature and thus a change in reflectivity. A probe beam is incident on the surface, reflecting off in proportion to the reflectivity. The amplitude of the pump beam is a continuous wave laser that is modulated sinusoidally and creates thermal waves in the material. The reflected probe beam thus also modulates sinusoidally at the same frequency. A phase delay occurs between the pump beam and the reflected probe beam, which is a function of the frequency, the geometry of the material, and the transport properties of the layers. The resultant data can be matched with theoretical equations to extract thermal characteristics of the system through inverse methods. Additionally, fiber-based FDTR devices have successfully determined thermal diffusivity with relatively simple instrumentation [59], [60]. Using fiber optics is desirable for the current work, due to the need for a FSW probe to be portable or remotely operating, robust, and non-contacting. This imposes some restrictions on how well the analytical thermal models match experimental conditions.

This paper will derive several semi-transparent, multi-layered thermal models for use with the FDTR method. The thermal quadrupole-based models will then be used to determine the optimal design configuration for a system to measure h in a FSW environment. Finally, the thermal model's ability to determine h will be validated by analyzing data from COMSOL simulations with limited radial bounds and linearly translation approximating the movement during a FSW process.

2. Analytical Models

Because of the multi-layered aspect of the experiment, potential methods were surveyed to determine h. Green's functions have been successfully used with thermal wave phenomena in general [61] and specifically with thermoreflectance techniques [62]. However, adding multiple layers is relatively arduous and even a simple two-layered geometry requires moderate computational resources. While using Green's function is possible, other methods were deemed easier. The 2D Fourier/Hankel transforms have also been used successfully [63], with relatively straightforward adaptation to multiple layers. This approach uses increasingly large determinant calculations, however, rapidly requiring a large amount of computational power as more layers are added. Thus, this approach was deemed unsuitable as well. The final method that was surveyed was thermal quadrupoles, which proved to be effective at modelling layered structures of varying configurations [64], [65] as well as determining material thermal properties [66]. Furthermore, it has proven to be readily capable of being modified to reduce computational requirements [67], as well been modified to determine interfacial

thermal contact conductance [68]. Thus, the thermal quadrupoles method was chosen as the method to be used.

2.1 Thermal Quadrupoles

The thermal quadrupoles method begins by taking the heat diffusion equation for heat transfer within a material [69]. The flux and temperature response can then be combined into a single matrix equation as a function of position. This equation is solved at the top and bottom of the layer, as shown in Figure 3a. Multiple layers can be related through the boundary condition of thermal contact conductance, which can be represented as a matrix. Heat loss due to convection on the surfaces can be accounted for as well, although these have been shown to be negligible at higher frequencies and with good thermal conductors [64]. Heat loss at the surfaces will be neglected and the surfaces assumed adiabatic. The thermal quadrupoles method can be easily extended to 2D systems using the Hankel or Fourier transforms. The thermal quadrupoles method has also been readily extended to semi-transparent layers [64], [65].

Salazar et al. [64] developed both the 1D and 2D general case for multiple layers under modulated plane and Gaussian illumination. However, the derivation of Salazar et al. placed the Q_1 (heat source) matrix with the $T_1(z = l_1)$ – temperature – matrix, resulting in the form $T_1(z = 0) = M_1 T_1(z = l_1) + M_1 Q_1$. Ordonez et al. [65] developed the 1D general case for multiple layers under modulated plane illumination in a different yet equivalent way to Salazar et al., resulting with the Q_1 matrix as distinct from the temperature response of the back end of the layer. In the current paper, the final derivation of Ordonez et al. is used for each 1D case because the Q_1 matrix components simplify under the assumptions that the layers are either completely transparent or completely opaque. Also in the current paper, a 2D case is derived, keeping the Q_1 matrix distinctly separate from the $T_1(z = l_1)$ matrix, maintaining the simplifying assumptions of opaque and transparent for the 2D case. These simplifications are necessary to maintain low computational requirements. Finally, a further derivation is made that determines the temperature response of an interior layer, maintaining simplifying assumptions and small computational requirements.

2.1.1 2D General Case

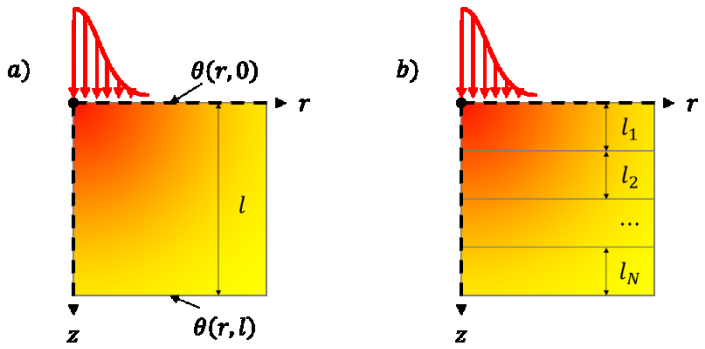

Figure 3. a) The 2D general case for the Gaussian distribution laser illuminated single-layer system. The layer is characterized by its thermal conductivity k, density ρ, specific heat c_p, thermal diffusivity $\alpha = k/\rho c_p$, optical absorption coefficient γ, and thickness l. The laser is characterized by the radius a when the intensity reaches $1/e^2$ and has a power P. b) The 2D general case for the Gaussian distribution laser illuminated multi-layer system of N layers. The layer i is characterized by its thermal conductivity k_i, density ρ_i, specific heat $c_{p,i}$, thermal diffusivity $\alpha_i = k_i/\rho_i c_{p,i}$, optical absorption coefficient γ_i, and thickness l_i. The laser is characterized by the radius a when the intensity reaches $1/e^2$ and has a power P_i.

For the 2D single-layer general case shown in Figure 3a, this derivation will initially follow that of Salazar et al. [64]. The 2D heat diffusion equation for this case is

$$\frac{\partial^2\theta(r,z)}{\partial r^2}+\frac{1}{r}\frac{\partial\theta(r,z)}{\partial r}+\frac{\partial^2\theta(r,z)}{\partial z^2}-\sigma^2\theta(r,z)=-\frac{Q}{k}, \tag{1}$$

where $\sigma=\sqrt{i\omega/\alpha}$ is the thermal wave vector, $Q=2P\gamma e^{-(2r^2/a^2)}e^{-\gamma z}/\pi k a^2$ is the Gaussian laser heat source, P is the power of the laser incident on the top of the layer, and $\theta(r,z)$ is the temperature response at radius r and depth z.

It can be easily shown that

$$\begin{bmatrix}\Theta(0)\\ \Phi(0)\end{bmatrix}=\begin{bmatrix}A & B\\ C & D\end{bmatrix}\begin{bmatrix}\Theta(l)\\ \Phi(l)\end{bmatrix}+\begin{bmatrix}U\\ V\end{bmatrix}, \tag{2}$$

where $A=D=\cosh(\beta l)$, $B=\sinh(\beta l)/k\beta$, $C=k\beta\sinh(\beta l)$, $U=y(0)\{1-[\cosh(\beta l)+\zeta\sinh(\beta l)]e^{-\gamma l}\}$, $V=k\beta\,y(0)\{\zeta-[\sinh(\beta l)+\zeta\cosh(\beta l)]e^{-\gamma l}\}$, $\zeta=\gamma/\beta$, and Φ is the flux in Hankel space. Note that Eq. (2) is different from that of Salazar et al. [64] and matches Ordonez et al. [65] in that the U and V matrix does not multiply with the quadrupoles matrix. Eq. (2) is completely analogous to the single-layer case developed by Ordonez et al. and a multi-layered structure can be developed exactly how Ordonez et al. developed it. The only difference is that the 2D case requires the reverse Hankel transform after the temperature in Hankel space is found.

An important simplification is that of opaqueness and transparency. As a layer becomes infinitely opaque ($\gamma\to\infty$), the values U and V simplify to 0 and $-P_1e^{-(u^2a^2/8)}/2\pi$, respectively. As a layer becomes infinitely transparent ($\gamma\to 0$), the values U and V both simplify to 0. It is noted that without these simplifications, U and V would approach infinity rapidly and render calculations useless. The full derivation is in Appendix A.

It can be shown that

$$J_1(0)=Z_N'\,J_N(l_N)+Q_N', \tag{3}$$

where $Z_N'=\prod_{n=1}^{N}M_nC_{n,n+1}$, $Q_N'=\prod_{n=1}^{N}Z_{n-1}'Q_n$, $C_{N,N+1}=1$, $Z_0'=1$,

$$M_n=\begin{bmatrix}A_n & B_n\\ C_n & D_n\end{bmatrix}, \tag{4}$$

$$Q_n=\begin{bmatrix}U_n\\ V_n\end{bmatrix}, \text{ and} \tag{5}$$

$$J_n(z)=\begin{bmatrix}\Theta_n(z)\\ \Phi_n(z)\end{bmatrix}, \tag{6}$$

$$C_{n,n+1}=\begin{bmatrix}1 & 1/h_{n,n+1}\\ 0 & 1\end{bmatrix}, \tag{7}$$

which is completely analogous to the derivation of Ordonez [65]. The full derivation is in Appendix A.

2.2 Potential Design Configurations

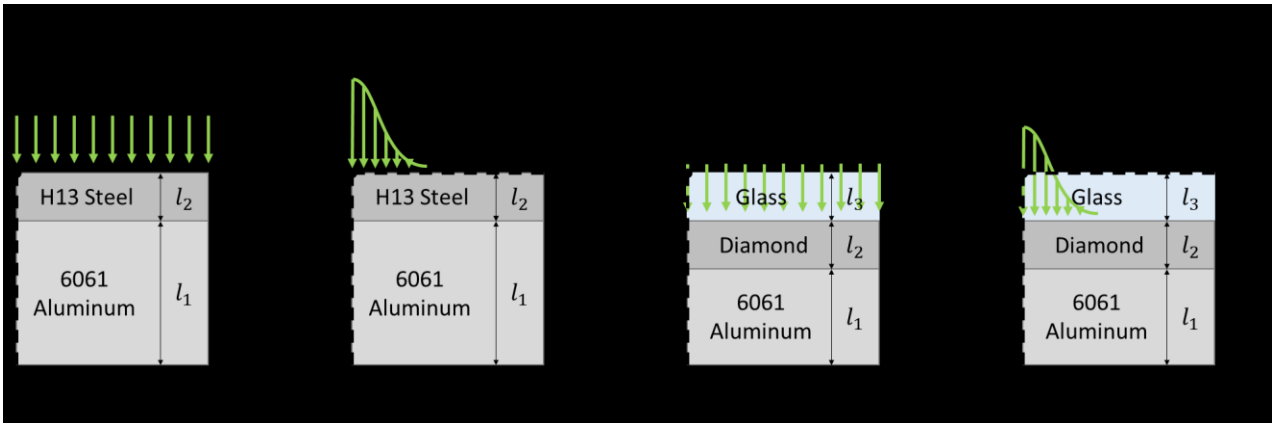

Figure 4. Configurations of four geometries surveyed for their potential use in a FDTR setup to determine the thermal contact conductance between a FSW tool and welded material interface.

We will survey the four specific cases as seen in Figure 4 to demonstrate why a multi-layered semi-transparent model was needed to determine the thermal contact conductance between a tool head and welded material interface. Case I is a semi-infinite two-layer system under plane illumination. Case II is a semi-infinite two-layer system under Gaussian illumination. These layered structures represent a plug that would be press fit into a hole drilled through the FSW tool to perform an FDTR measurement with a fiber optic probe placed in the tool head. Cases I and II use the same two-layer setup. Case III is a three-layer system under plane illumination. Case IV is a three-layer system under Gaussian illumination. Cases III and IV use the same three-layer setup and differ from Cases I and II in that their first layer is modelled as completely transparent at the pump and probe wavelengths, $550 - 750\ nm$. This is valid for the Eagle XG glass chosen for the transducer. The various parameters involved in each case are summarized in Table 1. The values of h analyzed are listed in Table 2. The next section will discuss optimization.

Table 1. Various parameters for Cases I-IV.

	Case I	Case II	Case III	Case IV
$l_3\ (mm)$	–	–	0.5	0.5
$l_2\ (mm)$	1	1	0.03	0.03
$l_1\ (mm)$	10	10	10	10
$k_3\ (W\ m^{-1}\ K^{-1})$	–	–	1.437	1.437
$k_2\ (W\ m^{-1}\ K^{-1})$	50.2	50.2	700	700
$k_1\ (W\ m^{-1}\ K^{-1})$	205	205	205	205
$\rho_3\ (kg\ m^{-3})$	–	–	2,380	2,380
$\rho_2\ (kg\ m^{-3})$	8,050	8,050	3,515	3,515
$\rho_1\ (kgm^{-3})$	2,700	2,700	2,700	2,700
$c_{p,3}\ (J\ kg^{-1}\ K^{-1})$	–	–	1,191	1,191
$c_{p,2}\ (J\ kg^{-1}\ K^{-1})$	502	502	51	51

$c_{p,1}\ (J\ kg^{-1}\ K^{-1})$	921	921	921	921
$\gamma_3\ (m^{-1})$	–	–	0	0
$\gamma_2\ (m^{-1})$	∞	∞	∞	∞
$\gamma_1\ (m^{-1})$	N/A	N/A	N/A	N/A
$d_{probe}\ (\mu m)$	110	110	110	110
$h_{2,3}\ (W\ m^{-2}\ K^{-1})$	–	–	$1e8$	$1e8$
$P_{laser}\ (mW)$	100	100	100	100
$r_{pump}\ (\mu m)$	5	5	5	5

Table 2. Thermal Contact Conductance at workpiece/tool interface ($Wm^{-2}K^{-1}$).

h_1	h_2	h_3	h_4	h_5	h_6
1,000	2,187	4,782	10,456	22,865	50,000

2.2.1 Case I

For Case I, the first layer is H13 steel (a common FSW tool alloy) with a thickness $l_2 = 1\ mm$ representing the most basic tool design. This was determined as the thinnest layer used in the tool head shoulder. The second layer is 6061 aluminum with a thickness $l_1 = 10\ mm$, representing a typical thickness of welded aluminum. The material properties used in this analysis are summarized in Table 1. The first layer is modelled as infinitely opaque. The equation used for Case I was derived from the results of Ordonez and is shown below:

$$\theta_2(0) = \frac{I_2}{2}\frac{\left(A_1A_2+C_1A_2{h_{2,1}}^{-1}+C_1B_2\right)}{\left(A_1C_2+C_1C_2{h_{2,1}}^{-1}+C_1D_2\right)}, \tag{8}$$

where $\theta_2(0)$ represents the periodic temperature response at the top layer where the probe laser emitted from the fiber optic would be. This equation is exact and requires very little computational power. The full derivation for Eq. (8)~~(8)~~ is included in Appendix B.

2.2.2 Case I Analysis

Figure 5a shows the various phase delays across a range of frequencies and thermal contact conductances, h, between layers for Case I. Meaningful phase difference between thermal contact conductances occurs below $10\ Hz$. Xing et al. [70] demonstrated that an error of around 3% occurs when the heating spot size is ten times larger than the thermal diffusion length, L_{th}. The thermal diffusion length is given by $L_{th} = \alpha/\pi f$, which is $600\ \mu m$ and $1.6\ mm$ for H13 steel and 6061 aluminum, respectively. This would require a heating spot size of $6\ mm$ at least at the $10\ Hz$ frequency, increasing in size as the frequency decreased. Since the geometry is limited to a maximum heating spot size of $2\ mm$, the 1D analytical case is unsuitable. Additionally, the pump probe radius is constrained to $5\ \mu m$ to reduce the need to focus the laser as it leaves the fiber optic. Benchmarks I and II are now introduced as the results obtained from COMSOL simulations modelling 3D FSW processes with the layered structure inserted as a plug into the tool. These Benchmarks use thermoplastic theory to model

the heat generated and model the linear translation of the tool. Material deformation, tool rotation, and temperature-dependent thermal properties aren't modelled in the Benchmarks. Benchmark I corresponds to Case I and Case II while Benchmark II corresponds to Case III and Case IV and will be discussed in Sections 2.2.5 to 2.2.8. As can be seen in Figure 5a, the Benchmark I phase delay curve greatly deviates from the 1D analytical phase delay curve, supporting the conclusion that Case I is unsuitable. Furthermore, the difference between phase delay curves for each h is negligible, showing that the two-layer setup with H13 and aluminum is unsuitable.

2.2.3 Case II

Case II is the same as Case I except with a 2D Gaussian distributed laser illuminating the top surface. It assumes the radial direction is semi-infinite. The equation for Case II is structurally identical to the equation for Case I, with the periodic temperature being represented in transform space. It was derived using the results of Eq. (3) and is shown below:

$$\Theta_2(0) = \frac{P_2 e^{-(u^2 a^2/8)}}{2\pi} \frac{(A_1A_2 + C_1A_2{h_{2,1}}^{-1} + C_1B_2)}{(A_1C_2 + C_1C_2{h_{2,1}}^{-1} + C_1D_2)}, \quad (9)$$

where $\Theta_2(0)$ representing the temperature in Hankel space and requiring the inverse Hankel Transform, and u as the Hankel transform variable. All other variables are identical to Case I with the exception that $V_2 = -P_2 e^{-(u^2 a^2/8)}/2\pi$ and σ_i is replaced with $\beta_n = \sqrt{u^2 + i\omega/\alpha_n}$. This equation requires numerical integration and requires moderate computational power. The full derivation for Eq. (9)~~(9)~~ is in Appendix B.

2.2.4 Case II Analysis

Figure 5b shows the various phase delay curves across a range of frequencies and thermal contact conductances between the FSW tool (layer 2) and the workpiece (layer 1) for varying situations. The "Analytical" curves were obtained from the analytical equations developed using the thermal quadrupoles method for the geometry of Case II. The "Numerical" curves were obtained with a 2D axisymmetric COMSOL model and validate the "Analytical" curves under simple conditions. This convention is used in Section 2.2.2 and continues through the current paper. The semi-infinite assumption in the radial direction is valid only for situations in which the flat geometry continues approximately five times further than the thermal diffusion length [71]. The frequencies of interest are below $10\ Hz$, where the thermal diffusion lengths for H13 and 6061 are $600\ \mu m$ and $1.6\ mm$, respectively. This requires a radial continuity of the flat geometry for at least $3\ mm$. The radial continuity is approximately $2\ mm$ until the curve of the tool is encountered and should align at higher frequencies, however, the frequencies of interest are below $10\ Hz$ and thus Case II is unsuitable. Figure 5b shows that the Benchmark I phase delay curve does indeed align with the phase delay curves of Case II at approximately $10\ Hz$ and higher, but doesn't align at lower frequencies, supporting the position that Case II is insufficient.

Since the phase delay curves align at higher frequencies for Case II and Benchmark I, a new layered structure is required to move the frequencies of interest to a higher frequency range.

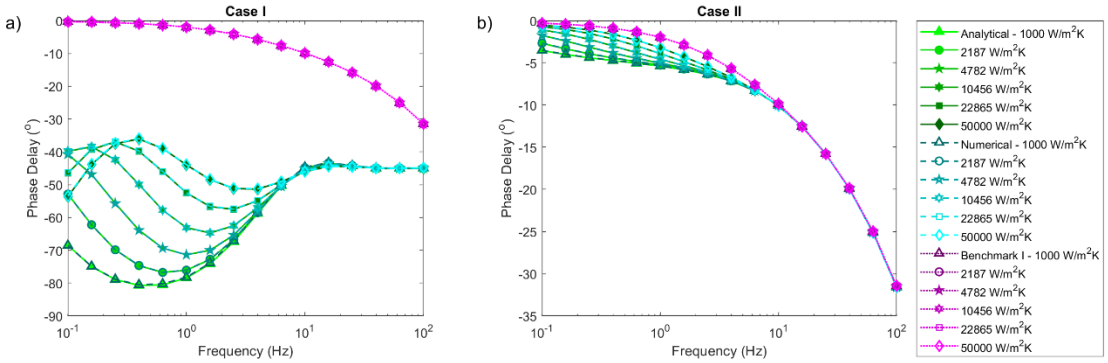

Figure 5. a) Phase delay curves across a range of thermal contact conductances, h, and frequencies for the analytical solution to Case I (filled in green shades) to the COMSOL generated simulation results (hollow blue shades). b) Phase delay curves across a range of thermal contact conductances and frequencies for the analytical solution to Case II (filled in green shades) to the COMSOL generated simulation results (hollow blue shades). Numerical solution with bounded radial geometry (filled in orange shades).

2.2.5 Case III

For Case III, the first layer is glass with a thickness $l_1 = 0.5\ mm$. This thickness was determined to be suitable to withstand the loads of FSW. The second layer is black diamond with a thickness $l_1 = 30\ \mu m$. Black diamond (tool quality) was chosen because it is a hard substance capable of surviving the extreme forces present at the tool head interface and is highly thermally conductive. The third layer is aluminum with a thickness $l_{al} = 10\ mm$, representing a typical thickness of welded aluminum. The material properties used in this analysis are summarized in Table 1. The first layer is modelled as completely transparent while the second layer is modelled as infinitely opaque.

Because the first layer is transparent, we are interested in the temperature response of the second layer. This temperature response can be developed from Ordonez et al. [65] similarly to Case I. The result is

$$\theta_2(0) = -V_2 \frac{\left(A_1A_2+C_1A_2{h_{2,1}}^{-1}+C_1B_2\right)\left(C_3{h_{3,2}}^{-1}+D_3\right)}{\Psi} \text{ with} \tag{10}$$

$$\Psi = \left(A_1A_2C_3 + A_1C_2C_3{h_{3,2}}^{-1} + A_1C_2D_3 + C_1A_2C_3{h_{2,1}}^{-1} + C_1C_2C_3{h_{3,2}}^{-1}{h_{2,1}}^{-1} + C_1C_2D_3{h_{2,1}}^{-1} + C_1B_2C_3 + C_1D_2C_3{h_{3,2}}^{-1} + C_1D_2D_3\right). \tag{11}$$

The full derivation of Eqs. (10)~~(10)~~ and (11)~~(11)~~ are included in Appendix B.

2.2.6 Case III Analysis

Figure 6a shows the various phase delays across a range of frequencies and thermal contact conductances between layers. Meaningful (being defined as those that are sensitive to changes in h) phase difference between thermal contact conductances occurs between 100 and $1{,}000\ Hz$. The thermal diffusion length is given by $L_{th} = \alpha/\pi f$, which is $40\ \mu m$, $1.1\ mm$, and $50\ \mu m$ for glass, black diamond, and 6061 aluminum, respectively, at $10\ Hz$. This would require a heating spot size of $11\ mm$ at least at $100\ Hz$. To ensure a 1D heat transfer assumption is valid, the layer thickness is $13\ \mu m$, $350\ \mu m$, and $160\ \mu m$ for glass, black diamond, and 6061 aluminum, respectively, at $1{,}000\ Hz$. This would require, at maximum, a heating spot size of $3.5\ mm$. This is unsuitable for the tool head and thus Case III is not sufficient. It should be noted, however, that if the black diamond layer could become

much thinner, the 1D assumption may be valid. This is not addressed in the current paper. The Benchmark II phase delay curves do not match with the phase delay curves of Case III, and thus the position that Case III is insufficient is supported.

2.2.7 Case IV

Case IV is the same as Case III except with a 2D Gaussian distributed laser illuminating the top surface. It assumes the radial direction is semi-infinite. The equation for Case IV is structurally identical to the equation for Case III, with the periodic temperature being represented in transform space. The equation was developed from Eq. (3) and is

$$\Theta_2(0) = -V_2 \frac{\left(A_1A_2+C_1A_2{h_{2,1}}^{-1}+C_1B_2\right)\left(C_3{h_{3,2}}^{-1}+D_3\right)}{\Psi} \text{ with} \tag{12}$$

$$\Psi = \left(A_1A_2C_3 + A_1C_2C_3{h_{3,2}}^{-1} + A_1C_2D_3 + C_1A_2C_3{h_{2,1}}^{-1} + C_1C_2C_3{h_{3,2}}^{-1}{h_{2,1}}^{-1} + C_1C_2D_3{h_{2,1}}^{-1} + C_1B_2C_3 + C_1D_2C_3{h_{3,2}}^{-1} + C_1D_2D_3\right). \tag{13}$$

with u as the Hankel transform variable. All other variables are identical to Case I with the exception that $V_2 = -P_2e^{-(u^2a^2/8)}/2\pi$ and σ_i is replaced with $\beta_n = \sqrt{u^2 + i\omega/\alpha_n}$. The full derivation of Eqs. (12)~~(12)~~ and (13)~~(13)~~ are included in Appendix B.

An additional analysis was done with a thin gold film transducer between the glass and black diamond layers and then compared to the results of Case IV. Negligible difference resulted, and as such, a nm thin gold film used as a thermoreflectance transducer was modeled as part of h at the tool and workpiece interface.

2.2.8 Case IV Analysis

Figure 6b shows the frequencies of interest, which are above $100\ Hz$, at which the thermal diffusion lengths are $40\ \mu m$, $1.1\ mm$, and $50\ \mu m$ for glass, black diamond, and 6061 aluminum, respectively. This requires a radial continuity of the flat geometry for at least $5\ mm$ assuming a homogenous 6061 aluminum material. The required radial continuity of the flat geometry decreases as the frequency increases. The effect of the layered structure is not directly analyzed, but it can be seen in Figure 6b that the Benchmark II phase delay curves align directly with the phase delay curves of Case IV. Thus, the layered structure appears to decrease the required radial continuity to below $2\ mm$ and Case IV is sufficient for the FSW geometry. Since the frequency range of interest is above the $10\ Hz$ rate of rotation of the tool head, error due to the tool rotation in a temperature field will be reduced. We will now optimize the layered structure of Case IV.

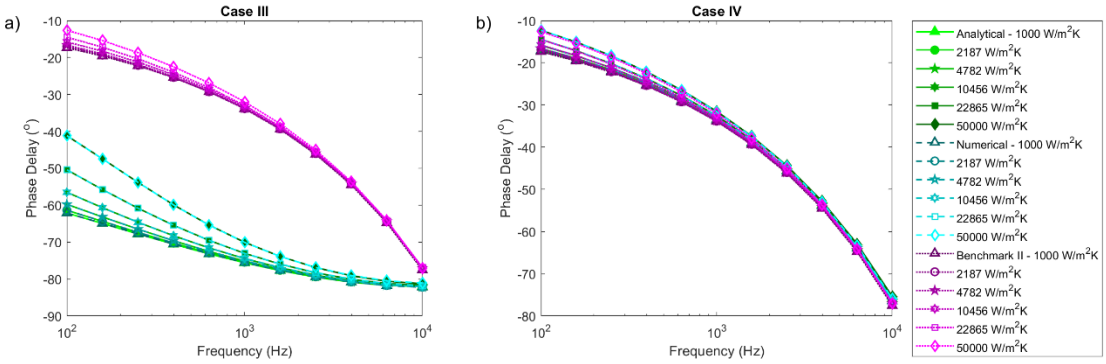

Figure 6. a) Phase delay curves across a range of thermal contact conductances and frequencies for the analytical solution to Case III (filled in green shades) to the COMSOL generated simulation results (hollow blue shades). b) Phase delay curves across a range of thermal contact conductances and frequencies for the analytical solution to Case IV (filled in green shades) to the COMSOL generated simulation results (hollow blue shades).

3. Sensitivity Analysis for design optimization

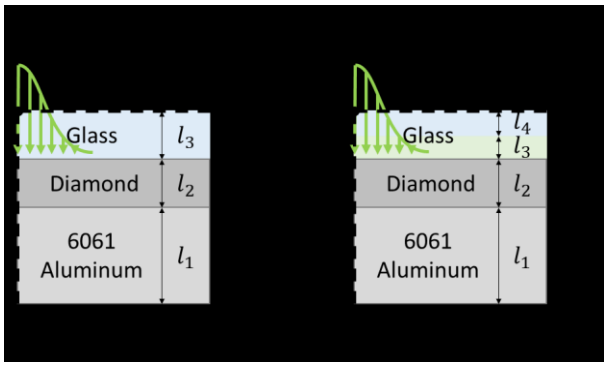

Figure 7. Configurations of two geometries to demonstrate sensitivity to various parameters in a FDTR setup to determine $h_{W/T}$ at the diamond/aluminum interface ($h_{1,2}$).

A fifth case, Case V, is presented here to compare with Case IV to determine and demonstrate an optimized design, as shown in Figure 7. The difference between Case IV and Case V is that Case V has an additional layer between the first and second layer of Case IV, with this additional layer having the same thermal properties as the other glass layer. Because the parameter of interest is the thermal interface conductance between the tool head and workpiece $(h_{1,2})$, we want as much heat flow through this interface as possible so we can detect it. This requires resistance to the heat flowing away from that interface. Tomimura et al. [72] showed that when a thin soft layer is placed between the interface of two harder materials, it results in a higher thermal contact conductance. The additional layer forces an interface between two hard materials, namely the glass, thus reducing the thermal contact conductance. Since the additional glass layer is so thin, it will act as a barrier to heat flow, directing more heat into the interface of interest.

We will define a phase spread term as what the difference in the phase delay at a given frequency for the range of conductances used is. This will reduce a 3d plot to a 2D plot and will show how sensitive the phase is to changes in a parameter. For the design of this device, we want the spread of these phase changes to be at a maximum so that we can successfully extract the h value during a test

The temperature amplitude is important because it will be easier to measure phase effects when the temperature response is greater, and if it is below a certain point, it will not be possible to detect the signal with the lock-in amplified. The phase spread is important because we will curve-fit experimental data to a theoretical phase delay curve to extract the thermal interface conductance. While the literature lists $1{,}000\ Wm^{-2}K^{-1}$ to $50{,}000\ Wm^{-2}K^{-1}$, the range of $10{,}000\ Wm^{-2}K^{-1}$ to $50{,}000\ Wm^{-2}K^{-1}$ was chosen to demonstrate sensitivity. Figure 8 presents the sensitivity of $h_{1,2}$ in cases IV and V to various parameters, which leads to an optimal design in Figure 9 to determine $h_{1,2}$. Table 3~~Table 2~~ at the end of this section summarizes the parameters used for the nominal and ideal parameter values for Cases IV and V.

3.1 Sensitivity Comparison

3.1.1 Topmost Layer Thickness

Figure 8a-b shows that the thickness of the topmost layer (transparent glass) has no effect across a range of values.

3.1.2 Opaque Layer Thickness

Figure 8c-d shows that as the thickness of the first opaque layer increases, both the temperature and phase difference effects become less pronounced. Case V has a greater sensitivity to decreasing thickness of the first opaque (diamond) layer.

3.1.3 Thermal Contact Conductance

Figure 8e-f shows that as the thermal contact conductance between the Black Diamond ~~(layers 2 and 3 for Cases IV and V, respectively)~~ and the glass layer immediately atop it decreases, the temperature effect increases slightly while the phase increase is more pronounced. Case V appears to have a slightly more pronounced phase difference at higher thermal contact conductances, which is desirable because the thermal contact conductance between the black diamond and glass layer immediately atop it is likely to be high, due to the thin reflective gold layer that is here.

3.1.4 Thermal Conductivity of third Layer

Figure 8g-h shows that as the thermal conductivity of the glass layer immediately atop the black diamond decreases, the temperature increases for Case IV. The temperature increases for Case V as well, but the phase difference behaves differently. At lower frequencies, there is less phase difference at lower thermal conductivities while more phase difference at higher thermal conductivities. There is hardly any difference at the lower frequencies, so assuming the phase difference increases at lower thermal conductivities is acceptable. Overall, Case V has higher temperatures and phase differences than Case IV.

3.1.5 Pump Laser Radius

Figure 8i-j shows that the pump laser radius size appears to have very little effect until it passes a critical value. For both cases, after the critical point, increasing pump laser size decreases temperature amplitude and increases phase difference.

3.1.6 Concentric Distance between Pump and Probe Lasers

Figure 8k-l shows that for both cases, as the distance between the pump and probe increases, the temperature amplitude decreases, and the phase difference increases. Case V has a more pronounced phase difference at lower frequencies, although the increment between distances is close to that of Case IV.

3.1.7 Pump Laser Power

Figure 8m-n shows that as the pump power increases, the phase response is unchanged within each case, but the temperature amplitude increases proportionally to the increase in power.

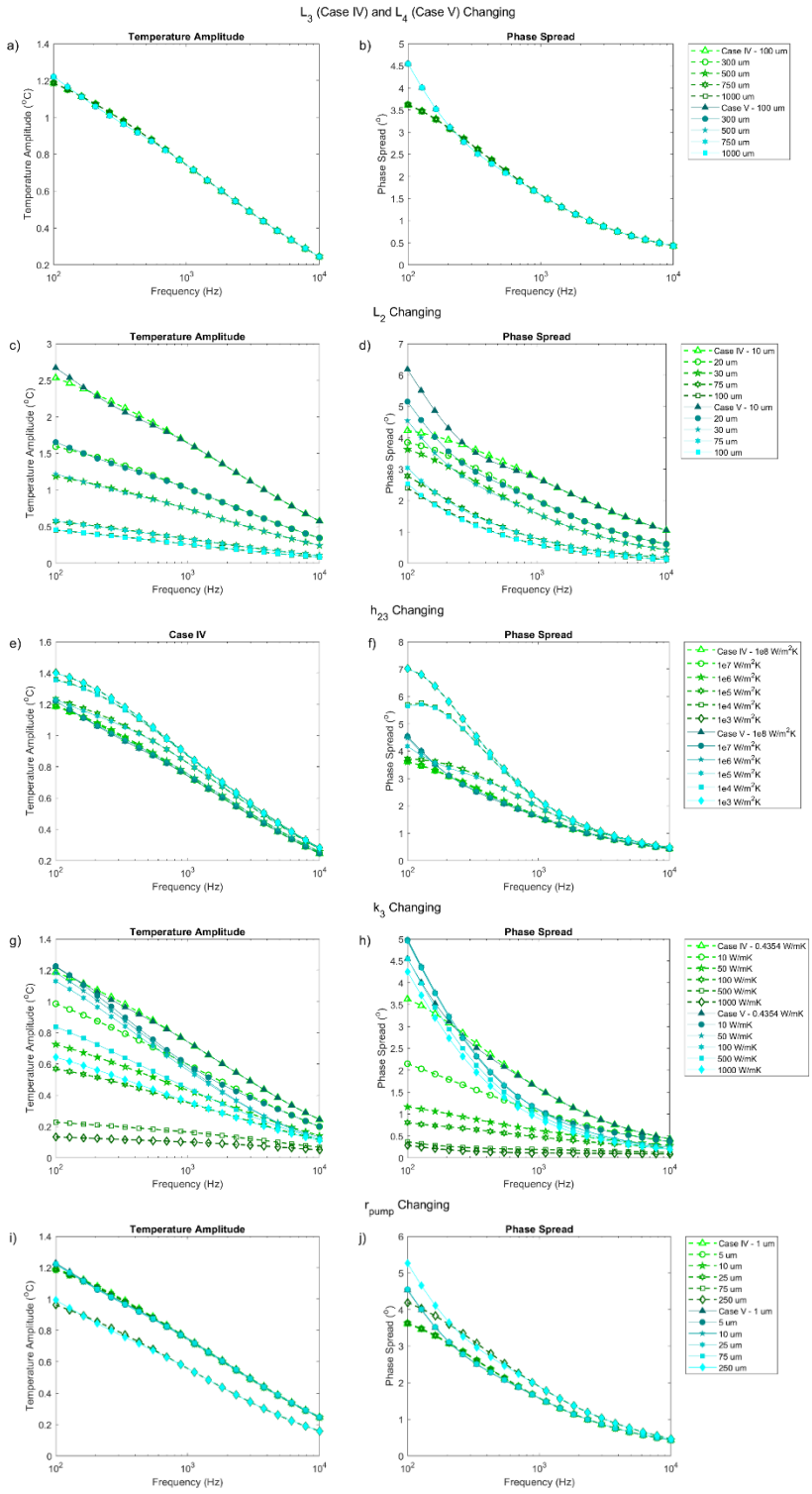
L_3 (Case IV) and L_4 (Case V) Changing
a)
Temperature Amplitude
Temperature Amplitude (°C)
Frequency (Hz)
b)
Phase Spread
Phase Spread (°)
Frequency (Hz)
Case IV - 100 um
300 um
500 um
750 um
1000 um
Case V - 100 um
300 um
500 um
750 um
1000 um
L_2 Changing
c)
Temperature Amplitude
Temperature Amplitude (°C)
Frequency (Hz)
d)
Phase Spread
Phase Spread (°)
Frequency (Hz)
Case IV - 10 um
20 um
30 um
75 um
100 um
Case V - 10 um
20 um
30 um
75 um
100 um
h_{23} Changing
e)
Case IV
Temperature Amplitude (°C)
Frequency (Hz)
f)
Phase Spread
Phase Spread (°)
Frequency (Hz)
Case IV - 1e8 W/m²K
1e7 W/m²K
1e6 W/m²K
1e5 W/m²K
1e4 W/m²K
1e3 W/m²K
Case V - 1e8 W/m²K
1e7 W/m²K
1e6 W/m²K
1e5 W/m²K
1e4 W/m²K
1e3 W/m²K
k_3 Changing
g)
Temperature Amplitude
Temperature Amplitude (°C)
Frequency (Hz)
h)
Phase Spread
Phase Spread (°)
Frequency (Hz)
Case IV - 0.4354 W/mK
10 W/mK
50 W/mK
100 W/mK
500 W/mK
1000 W/mK
Case V - 0.4354 W/mK
10 W/mK
50 W/mK
100 W/mK
500 W/mK
1000 W/mK
r_{pump} Changing
i)
Temperature Amplitude
Temperature Amplitude (°C)
Frequency (Hz)
j)
Phase Spread
Phase Spread (°)
Frequency (Hz)
Case IV - 1 um
5 um
10 um
25 um
75 um
250 um
Case V - 1 um
5 um
10 um
25 um
75 um
250 um

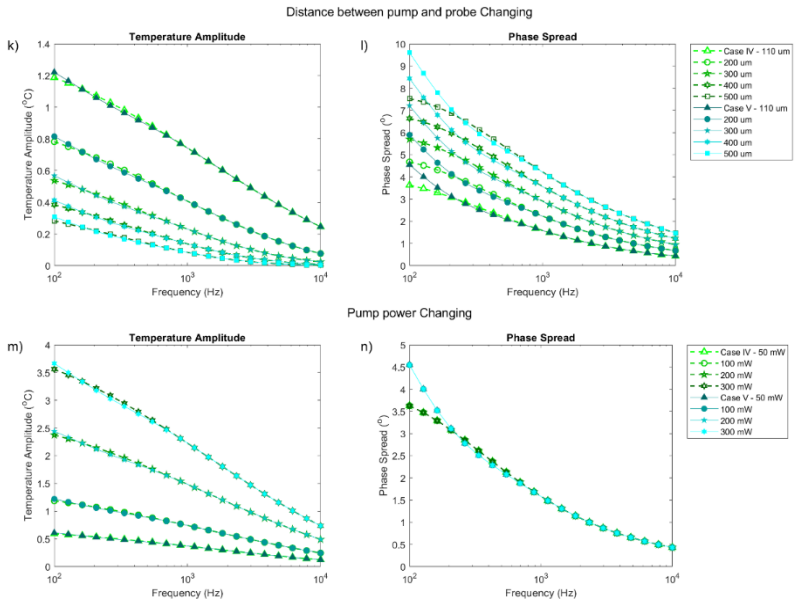

Figure 8. Sensitivity of Cases IV and V to a-b) the thickness of the uppermost glass layer, c-d) the thickness of the first opaque layer, e-f) the thermal contact conductance between the first opaque layer and the transparent layer immediately above it, g-h) the thermal conductivity of the transparent layer immediately atop the first opaque layer, i-j) the radius of the pump laser, k-l) the distance between the pump and probe laser, and m-n) the pump power changing.

3.1.8 Summary of Sensitive Parameters

The most sensitive parameters include the thickness of the black diamond layers, the thermal contact conductance between the opaque and transparent layers, the thermal conductivity of the transparent layer touching the opaque layer, the concentric distance between pump and probe lasers, and the pump laser power. These parameters were all chosen in the ideal configuration to maximize phase and temperature responses, except for thermal contact conductance which cannot be readily chosen and instead will be assumed a maximum, the likely worst-case scenario. The ideal parameters for each case are summarized in Table 3~~Table 2~~.

3.2 Optimal Design

Figure 9 compares the temperature amplitude and phase difference response of the nominal to ideal parameters for Cases IV and V. The temperature amplitude for both cases' ideal parameters is greater across most of the frequency range. The phase difference for both cases' ideal parameters are well above those of the nominal parameters. Case V has a more pronounced temperature response and a much more pronounced phase difference response compared to Case IV, demonstrating the superior configuration of Case V.

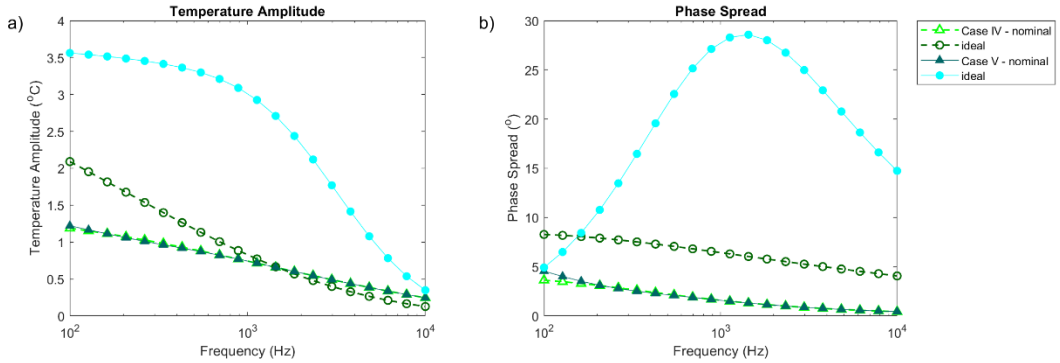

Figure 9. A comparison between the nominal and ideal parameters for Cases IV and V (based on the parameters in Table 3~~Table 2~~).

Table 3. Parameters for nominal and ideal parameters for Cases IV and V.

	Case IV - Nominal	Case IV - Ideal	Case V - Nominal	Case V - Validated	Case V - Ideal
$l_4\ (mm)$	–	–	0.5	2	2
$l_3\ (mm)$	0.5	0.25	0.03	0.06	0.001
$l_2\ (mm)$	0.03	0.001	0.03	0.06	0.001
$l_1\ (mm)$	10	10	10	10	10
$k_4\ (W\ m^{-1}\ K^{-1})$	–	–	1.437	1.437	1.437
$k_3\ (W\ m^{-1}\ K^{-1})$	1.437	1.437	1.437	1.437	1.437
$k_2\ (W\ m^{-1}\ K^{-1})$	700	700	700	700	700
$k_1\ (W\ m^{-1}\ K^{-1})$	205	205	205	205	205
$\rho_4\ (kg\ m^{-3})$	–	–	2,380	2,380	2,380
$\rho_3\ (kg\ m^{-3})$	2,380	2,380	2,380	2,380	2,380
$\rho_2\ (kg\ m^{-3})$	3,515	3,515	3,515	3,515	3,515
$\rho_1\ (kg\ m^{-3})$	2,700	2,700	2,700	2,700	2,700
$c_{p,4}\ (J\ kg^{-1}\ K^{-1})$	–	–	1,191	1,191	1,191
$c_{p,3}\ (J\ kg^{-1}\ K^{-1})$	1,191	1,191	1,191	1,191	1,191
$c_{p,2}\ (J\ kg^{-1}\ K^{-1})$	510	510	510	510	510
$c_{p,1}\ (J\ kg^{-1}\ K^{-1})$	921	921	921	921	921
$\gamma_4\ (m^{-1})$	–	–	0	0	0
$\gamma_3\ (m^{-1})$	0	0	0	0	0
$\gamma_2\ (m^{-1})$	∞	∞	∞	∞	∞
$\gamma_1\ (m^{-1})$	N/A	N/A	N/A	N/A	N/A
$d_{probe}\ (\mu m)$	110	250	110	110	250

$h_{3,2}\ (W\ m^{-2}\ K^{-1})$	$1e8$	$1e8$	$1e8$	$1e8$	$1e8$
$P_{laser}\ (mW)$	100	150	100	1000	150
$h_{4,3}\ (W\ m^{-2}\ K^{-1})$	–	–	$1e3$	$1e3$	$1e3$
$r_{pump}\ (\mu m)$	5	5	5	5	5

4. Thermal Model Validation from COMSOL Simulation and Tool Head Design

The Case V validated parameters were simulated in COMSOL with two different Benchmarks, Benchmark III and Benchmark IV, as shown in Figure 10. Benchmark III is a simple static model simulating the layered structure with radial constraints while Benchmark IV simulates the rotational motion of the FSW tool. This motion is simulated with a linear velocity of $0.5873\ m/s$, which is approximately what the tangential velocity would be in the FSW tool at the point where the probe is. Figure 11 a) shows the geometry, mesh, and temperature field of Benchmark III. Figure 11 b) shows the geometry, mesh, and temperature field of the top of the linearly translating layer of Benchmark IV. The temperature field of Figure 11 b) confirms that the linear translation was accounted for in the COMSOL model. The Case V Ideal parameters weren't used due to mesh density requirements for such thin layers ($1\ \mu m$). As can be seen in Figure 10, The Case V validated parameters matched closely with both Benchmark III and Benchmark IV, suggesting that this layered structure is unaffected by the radial boundary requirements and rotational motion of the FSW tool, and thus is a suitable technique for measuring $h_{W/T}$ during a FSW operation. The tool head design used in the Benchmark III/Case V nominal parameters validation simulation is shown in Figure 11 c).

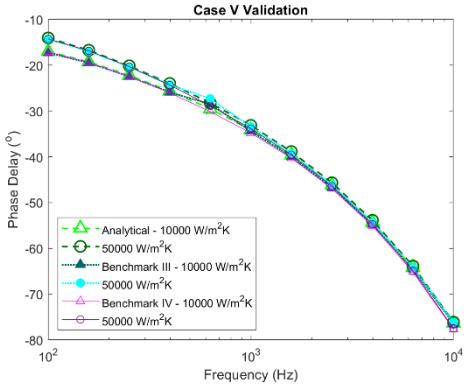

Figure 10. Phase delay curves from the analytical expression for Case V Validated parameters, Benchmark III, and Benchmark IV.

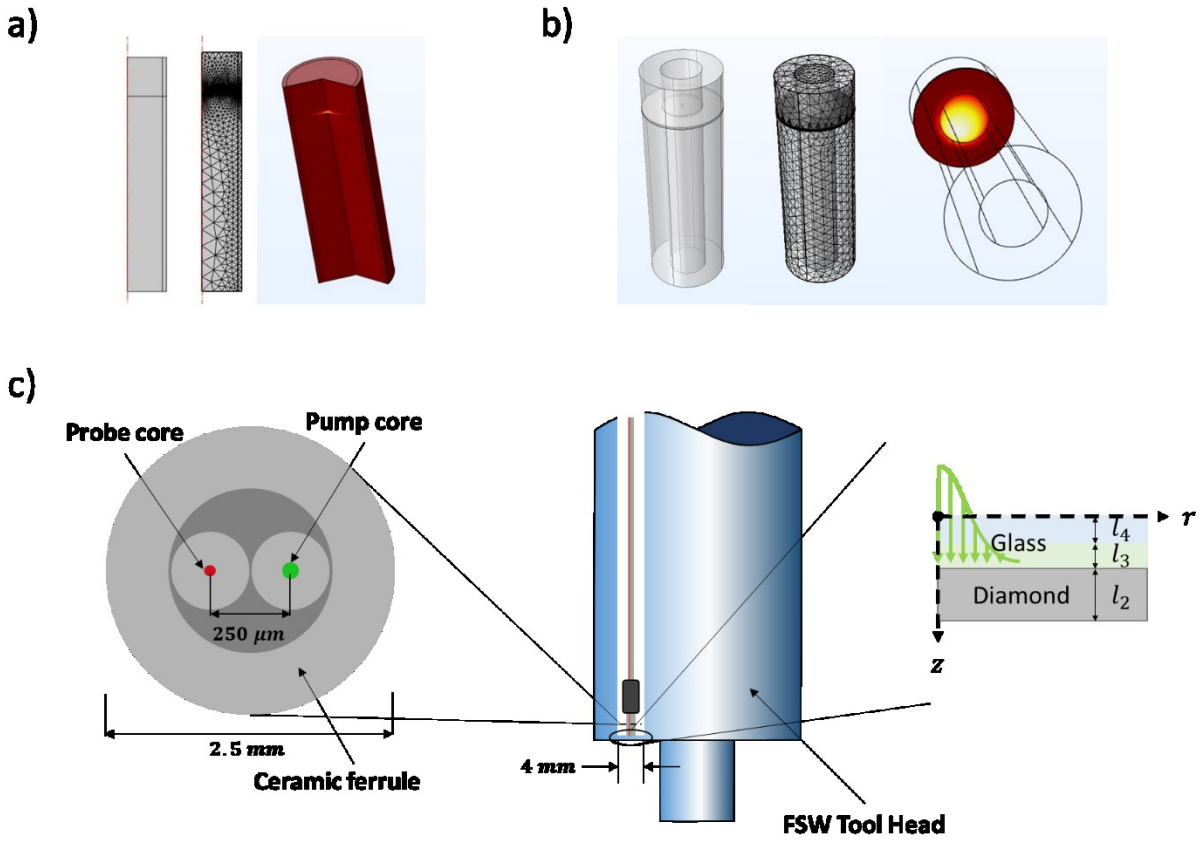

Figure 11. a) Benchmark III geometry, mesh, and temperature field of radially constrained boundary, b) Benchmark IV geometry, mesh, and temperature field on the top surface of the linearly translating layer, and c) FSW tool head design with probe cross section and layered structure (based on parameters from Table 3, Case V – Ideal).

5. Conclusion

A method for measuring the heat transfer coefficient between a spinning friction stir welding tool and a metal workpiece has been proposed and studied numerically. The best design configuration emerging from the study consists of a layer of clear glass, a second layer of clear glass, opaque diamond, and then aluminum. This layered structure will be fit into the FSW tool as a plug, allowing FDTR tests to be performed during FSW processes and extracting the relevant information of the actual process. The relatively low thermal contact conductance between the two glass layers acts as a barrier to heat flowing into the first thicker glass layer, directing the heat to flow into the diamond/aluminum interface. This is necessary since this is the interface of interest and requires as much heat as possible to flow through it to characterize the ~~thermal contact conductance~~heat transfer coefficient. The Case V ideal parameters maximize the effect of the ~~thermal contact conductance~~heat transfer coefficient at the diamond/aluminum interface and thus allow the inverse extraction of it when compared to the theoretical equations of Case V. The most sensitive parameters were the thicknesses of the layers directly touching the surface at which the laser is incident, as well as the thermal conductivity of the transparent layer in contact with the opaque layer. The probe distance and pump radius were more parameters for fine-tuning response. Future efforts include experimentally validating the Case IV and Case V equations in a simplified vice FDTR setup that simulates the pressures expected during FSW processes as well as in a high-temperature environment at ambient pressure. The effect of both the

isolated pressure and the isolated temperature compared to the Case IV and Case V equations will be analyzed and quantified. These validations will provide further proof that the device optimized in the current paper can measure the heat transfer coefficient during FSW operations. Once this validation has occurred, experiments utilizing a full FDTR FSW setup will provide final validation that the device works as presented. ~~Experimental work will be done to physically validate Case V (and Case IV) in a steady-state vice, after which a full FSW setup will be tested.~~

~~A~~In addition~~ally~~ to FSW applications, researchers can use these results as a reference in designing their own analytical model for an FDTR measurement inside other systems, such as an end mill and lathe.

6. Acknowledgements

This material is based upon work supported by the National Science Foundation under Grant No. 1935767.

[1] M. Mehta, K. Chatterjee, and A. De, “Monitoring torque and traverse force in friction stir welding from input electrical signatures of driving motors,” *Sci. Technol. Weld. Join.*, vol. 18, no. 3, pp. 191–197, Apr. 2013, doi: 10.1179/1362171812Y.0000000084.
[2] C. S. W. G. K. Padhy and C. S. W. G. K. Padhy, “Friction stir based welding and processing technologies - processes, parameters, microstructures and applications: A review,” *J. Mater. Sci. Technol.*, vol. 34, no. 1, pp. 1–38, Feb. 2018, doi: 10.1016/j.jmst.2017.11.029.
[3] I. M. Norris, W. M. Thomas, J. Martin, and D. J. Staines, “Friction Stir Welding: Processes and Recent Developments.” https://www.twi-global.com/technical-knowledge/published-papers/friction-stir-welding-process-variants-and-recent-industrial-developments-october-2007.aspx (accessed Jul. 18, 2020).
[4] R. S. Mishra and Z. Ma, “Friction stir welding and processing,” *Mater. Sci. Eng. R Rep.*, vol. 50, no. 1–2, pp. 1–78, 2005.
[5] P. L. Threadgill, A. J. Leonard, H. R. Shercliff, and P. J. Withers, “Friction stir welding of aluminium alloys,” *Int. Mater. Rev.*, vol. 54, no. 2, pp. 49–93, Mar. 2009, doi: 10.1179/174328009X411136.
[6] A. C. F. Silva, J. De Backer, and G. Bolmsjö, “Temperature measurements during friction stir welding,” *Int. J. Adv. Manuf. Technol.*, vol. 88, no. 9, pp. 2899–2908, Feb. 2017, doi: 10.1007/s00170-016-9007-4.
[7] S. Verma, J. P. Misra, and M. Gupta, “Study of Temperature Distribution During FSW of Aviation Grade AA6082,” in *Manufacturing Engineering*, 2019, pp. 185–202.
[8] A. Fehrenbacher, J. R. Schmale, M. R. Zinn, and F. E. Pfefferkorn, “Measurement of Tool-Workpiece Interface Temperature Distribution in Friction Stir Welding,” *J. Manuf. Sci. Eng.*, vol. 136, no. 2, pp. 021009-021009–8, Jan. 2014, doi: 10.1115/1.4026115.
[9] W. J. Arbegast, “A flow-partitioned deformation zone model for defect formation during friction stir welding,” *Scr. Mater.*, vol. 58, no. 5, pp. 372–376, Mar. 2008, doi: 10.1016/j.scriptamat.2007.10.031.
[10] M. Miles, U. Karki, and Y. Hovanski, “Temperature and Material Flow Prediction in Friction-Stir Spot Welding of Advanced High-Strength Steel,” *JOM*, vol. 66, no. 10, pp. 2130–2136, Oct. 2014, doi: 10.1007/s11837-014-1125-6.
[11] Y. J. Chao, X. Qi, and W. Tang, “Heat Transfer in Friction Stir Welding—Experimental and Numerical Studies,” *J. Manuf. Sci. Eng.*, vol. 125, no. 1, pp. 138–145, Feb. 2003, doi: 10.1115/1.1537741.
[12] M. Khandkar, J. A. Khan, and A. P. Reynolds, “Prediction of temperature distribution and thermal history during friction stir welding: input torque based model,” *Sci. Technol. Weld. Join.*, vol. 8, no. 3, pp. 165–174, 2003.
[13] M. Yu, W. Y. Li, J. L. Li, and Y. J. Chao, “Modelling of entire friction stir welding process by explicit finite element method,” *Mater. Sci. Technol.*, vol. 28, no. 7, pp. 812–817, Jul. 2012, doi: 10.1179/1743284711Y.0000000087.
[14] S. B. Aziz, M. W. Dewan, D. J. Huggett, M. A. Wahab, A. M. Okeil, and T. W. Liao, “A Fully Coupled Thermomechanical Model of Friction Stir Welding (FSW) and Numerical Studies on Process Parameters of Lightweight Aluminum Alloy Joints,” *Acta Metall. Sin. Engl. Lett.*, vol. 31, no. 1, Art. no. 1, Jan. 2018, doi: 10.1007/s40195-017-0658-4.
[15] T. Nakamura, T. Obikawa, E. Yukutake, S. Ueda, and I. Nishizaki, “Tool Temperature and Process Modeling of Friction Stir Welding,” *Mod. Mech. Eng.*, vol. 08, no. 01, Art. no. 01, 2018, doi: 10.4236/mme.2018.81006.
[16] E. dos S. Magalhaes, C. P. da Silva, A. L. F. Lima e Silva, and S. M. M. Lima e Silva, “An alternative approach to thermal analysis using inverse problems in aluminum alloy welding,” *Int. J. Numer. Methods Heat Fluid Flow*, vol. 27, no. 3, pp. 561–574, Jan. 2017, doi: 10.1108/HFF-03-2016-0106.
[17] N. Contuzzi, S. L. Campanelli, G. Casalino, and A. D. Ludovico, “On the role of the Thermal Contact Conductance during the Friction Stir Welding of an AA5754-H111 butt joint,” *Appl. Therm. Eng.*, vol. 104, pp. 263–273, Jul. 2016, doi: 10.1016/j.applthermaleng.2016.05.071.

[18] J. h. Hattel, M. Stolpe, and A. Larsen, “Estimating the workpiece-backing plate heat transfer coefficient in friction stirwelding,” *Eng. Comput.*, vol. 29, no. 1, Art. no. 1, Jan. 2012, doi: 10.1108/02644401211190573.
[19] R. Nandan, T. DebRoy, and H. K. D. H. Bhadeshia, “Recent advances in friction-stir welding – Process, weldment structure and properties,” *Prog. Mater. Sci.*, vol. 53, no. 6, pp. 980–1023, Aug. 2008, doi: 10.1016/j.pmatsci.2008.05.001.
[20] CemC. Tutum, K. Deb, and JesperH. Hattel, “Multi-Criteria Optimization in Friction Stir Welding Using a Thermal Model with Prescribed Material Flow,” *Mater. Manuf. Process.*, vol. 28, no. 7, pp. 816–822, Jul. 2013, doi: 10.1080/10426914.2012.736654.
[21] P. Biswas and N. R. Mandal, “Effect of Tool Geometries on Thermal History of FSW of AA1100,” *Weld. J.*, vol. 90, no. 7, p. 129.s-135.s, Jul. 2011.
[22] B. G. Kıral, M. Tabanoğlu, and H. T. Serindağ, “Finite Element Modeling of Friction Stir Welding in Aluminum Alloys Joint,” *Math. Comput. Appl.*, vol. 18, no. 2, Art. no. 2, Aug. 2013, doi: 10.3390/mca18020122.
[23] T. Dickerson, Q. Shi, and H. R. Shercliff, “Heat flow into friction stir welding tools,” in *4th international symposium on friction stir welding, Park City, Utah, USA*, 2003, pp. 14–16.
[24] Y. Pan and D. Lados, “Friction Stir Welding in Wrought and Cast Aluminum Alloys: Heat Transfer Modeling and Thermal History Analysis,” *Metall. Mater. Trans. Part A*, vol. 48, no. 2, pp. 722–734, Feb. 2017, doi: 10.1007/s11661-016-3865-0.
[25] L. Shi and C. S. Wu, “Transient model of heat transfer and material flow at different stages of friction stir welding process,” *J. Manuf. Process.*, vol. 25, pp. 323–339, Jan. 2017, doi: 10.1016/j.jmapro.2016.11.008.
[26] M. Rosochowska, K. Chodnikiewicz, and R. Balendra, “A new method of measuring thermal contact conductance,” *J. Mater. Process. Technol.*, vol. 145, no. 2, pp. 207–214, Jan. 2004, doi: 10.1016/S0924-0136(03)00671-X.
[27] M. Z. H. Khandkar, J. A. Khan, A. P. Reynolds, and M. A. Sutton, “Predicting residual thermal stresses in friction stir welded metals,” *J. Mater. Process. Technol.*, vol. 174, no. 1, pp. 195–203, May 2006, doi: 10.1016/j.jmatprotec.2005.12.013.
[28] H. Schmidt and J. Hattel, “A local model for the thermomechanical conditions in friction stir welding,” *Model. Simul. Mater. Sci. Eng.*, vol. 13, no. 1, Art. no. 1, Dec. 2004, doi: 10.1088/0965-0393/13/1/006.
[29] M. Song and R. Kovacevic, “Heat transfer modelling for both workpiece and tool in the friction stir welding process: A coupled model,” *Proc. Inst. Mech. Eng. Part B J. Eng. Manuf.*, vol. 218, no. 1, Art. no. 1, Jan. 2004, doi: 10.1243/095440504772830174.
[30] M. R. Sonne, C. C. Tutum, J. H. Hattel, A. Simar, and B. de Meester, “The effect of hardening laws and thermal softening on modeling residual stresses in FSW of aluminum alloy 2024-T3,” *J. Mater. Process. Technol.*, vol. 213, no. 3, pp. 477–486, Mar. 2013, doi: 10.1016/j.jmatprotec.2012.11.001.
[31] V. Soundararajan, S. Zekovic, and R. Kovacevic, “Thermo-mechanical model with adaptive boundary conditions for friction stir welding of Al 6061,” *Int. J. Mach. Tools Manuf.*, vol. 45, no. 14, pp. 1577–1587, Nov. 2005, doi: 10.1016/j.ijmachtools.2005.02.008.
[32] G. A. Moraitis and G. N. Labeas, “Residual stress and distortion calculation of laser beam welding for aluminum lap joints,” *J. Mater. Process. Technol.*, vol. 198, no. 1, pp. 260–269, Mar. 2008, doi: 10.1016/j.jmatprotec.2007.07.013.
[33] M. Boukraa, N. Lebaal, A. Mataoui, A. Settar, M. Aissani, and N. Tala-Ighil, “Friction stir welding process improvement through coupling an optimization procedure and three-dimensional transient heat transfer numerical analysis,” *J. Manuf. Process.*, vol. 34, pp. 566–578, Aug. 2018, doi: 10.1016/j.jmapro.2018.07.002.

[34] V. Farajkhah and C. G. Soares, “Finite element study on the ultimate strength of aluminum plates joined by friction stir welding,” in *Progress in the Analysis and Design of Marine Structures*, CRC Press, 2017, pp. 609–616.
[35] M. Bachmann, J. Carstensen, L. Bergmann, J. dos Santos, C. Wu, and M. Rethmeier, “Numerical simulation of thermally induced residual stresses in friction stir welding of aluminum alloy 2024-T3 at different welding speeds,” *Int. J. Adv. Manuf. Technol.*, vol. 91, no. 1–4, pp. 1443–1452, Jul. 2017, doi: 10.1007/s00170-016-9793-8.
[36] T. Nakamura, T. Obikawa, I. Nishizaki, M. Enomoto, and Z. Fang, “Friction Stir Welding of Non-Heat-Treatable High-Strength Alloy 5083-O,” *Metals*, vol. 8, no. 4, Art. no. 4, Apr. 2018, doi: 10.3390/met8040208.
[37] G. Buffa, A. Ducato, and L. Fratini, “Numerical procedure for residual stresses prediction in friction stir welding,” *Finite Elem. Anal. Des.*, vol. 47, no. 4, pp. 470–476, Apr. 2011, doi: 10.1016/j.finel.2010.12.018.
[38] N. Babu, N. Karunakaran, and V. Balasubramanian, “Numerical predictions and experimental investigation of the temperature distribution of friction stir welded AA 5059 aluminium alloy joints,” *Int. J. Mater. Res.*, vol. 108, no. 1, Art. no. 1, Jan. 2017, doi: 10.3139/146.111448.
[39] M. I. Costa, C. Leitão, and D. M. Rodrigues, “Parametric study of friction stir welding induced distortion in thin aluminium alloy plates: A coupled numerical and experimental analysis,” *Thin-Walled Struct.*, vol. 134, pp. 268–276, Jan. 2019, doi: 10.1016/j.tws.2018.10.027.
[40] C. C. Tutum and J. H. Hattel, “Numerical optimisation of friction stir welding: review of future challenges,” *Sci. Technol. Weld. Join.*, vol. 16, no. 4, pp. 318–324, 2011.
[41] P. A. Colegrove and H. R. Shercliff, “Experimental and numerical analysis of aluminium alloy 7075-T7351 friction stir welds,” *Sci. Technol. Weld. Join.*, vol. 8, no. 5, pp. 360–368, Oct. 2003, doi: 10.1179/136217103225005534.
[42] A. Al-Roubaiy, S. Nabat, and A. Batako, “Experimental and theoretical analysis of friction stir welding of Al-Cu joints,” *Int. J. Adv. Manuf. Technol.*, vol. 71, no. 9–12, pp. 1631–1642, Apr. 2014, doi: 10.1007/s00170-013-5563-z.
[43] B. Haddag, S. Atlati, M. Nouari, and M. Zenasni, “Analysis of the heat transfer at the tool–workpiece interface in machining: determination of heat generation and heat transfer coefficients,” *Heat Mass Transf.*, vol. 51, no. 10, pp. 1355–1370, Oct. 2015, doi: 10.1007/s00231-015-1499-1.
[44] V. Norouzifard and M. Hamedi, “Experimental determination of the tool–chip thermal contact conductance in machining process,” *Int. J. Mach. Tools Manuf.*, vol. 84, pp. 45–57, Sep. 2014, doi: 10.1016/j.ijmachtools.2014.04.003.
[45] R. Dou, T. Ge, X. Liu, and Z. Wen, “Effects of contact pressure, interface temperature, and surface roughness on thermal contact conductance between stainless steel surfaces under atmosphere condition,” *Int. J. Heat Mass Transf.*, vol. 94, pp. 156–163, Mar. 2016, doi: 10.1016/j.ijheatmasstransfer.2015.11.069.
[46] P. Zhang, Y. Xuan, and Q. Li, “A high-precision instrumentation of measuring thermal contact resistance using reversible heat flux,” *Exp. Therm. Fluid Sci.*, vol. 54, pp. 204–211, Apr. 2014, doi: 10.1016/j.expthermflusci.2013.12.012.
[47] X. Zhang, P. Z. Cong, and M. Fujii, “A Study on Thermal Contact Resistance at the Interface of Two Solids,” *Int. J. Thermophys.*, vol. 27, no. 3, pp. 880–895, May 2006, doi: 10.1007/s10765-006-0064-z.
[48] B. Sponagle and D. Groulx, “Measurement of thermal interface conductance at variable clamping pressures using a steady state method,” *Appl. Therm. Eng.*, vol. 96, pp. 671–681, Mar. 2016, doi: 10.1016/j.applthermaleng.2015.12.010.
[49] T. Tong and A. Majumdar, “Reexamining the 3-omega technique for thin film thermal characterization,” *Rev. Sci. Instrum.*, vol. 77, no. 10, p. 104902, Oct. 2006, doi: 10.1063/1.2349601.

[50] H.-C. Chien, D.-J. Yao, M.-J. Huang, and T.-Y. Chang, “Thermal conductivity measurement and interface thermal resistance estimation using SiO2 thin film,” *Rev. Sci. Instrum.*, vol. 79, no. 5, p. 054902, May 2008, doi: 10.1063/1.2927253.
[51] S.-M. Lee *et al.*, “Thermal Conductivity and Thermal Boundary Resistances of ALD Al2O3 Films on Si and Sapphire,” *Int. J. Thermophys.*, vol. 38, no. 12, p. 176, Oct. 2017, doi: 10.1007/s10765-017-2308-5.
[52] C. Fieberg and R. Kneer, “Determination of thermal contact resistance from transient temperature measurements,” *Int. J. Heat Mass Transf.*, vol. 51, no. 5, pp. 1017–1023, Mar. 2008, doi: 10.1016/j.ijheatmasstransfer.2007.05.004.
[53] N. D. Milošević, M. Raynaud, and K. D. Maglić, “Simultaneous Estimation of the Thermal Diffusivity and Thermal Contact Resistance of Thin Solid Films and Coatings Using the Two-Dimensional Flash Method,” *Int. J. Thermophys.*, vol. 24, no. 3, pp. 799–819, May 2003, doi: 10.1023/A:1024000602687.
[54] N. D. Milošević, “Determination of Transient Thermal Interface Resistance Between Two Bonded Metal Bodies using the Laser-Flash Method,” *Int. J. Thermophys.*, vol. 29, no. 6, pp. 2072–2087, Dec. 2008, doi: 10.1007/s10765-008-0378-0.
[55] K. Kagata, K. Kageyama, S. Kinoshita, and A. Yoshida, “Evaluation of Thermal Contact Resistance Between Two Solid Surfaces Using Photoacoustic Technique,” *Int. J. Thermophys.*, vol. 41, no. 9, p. 131, Jul. 2020, doi: 10.1007/s10765-020-02717-5.
[56] F. Mercuri *et al.*, “Depth-Resolved Analysis of Double-Layered Cultural Heritage Artifacts by Pulsed Thermography,” *Int. J. Thermophys.*, vol. 41, no. 1, p. 6, Dec. 2019, doi: 10.1007/s10765-019-2587-0.
[57] P. Jiang, X. Qian, and R. Yang, “Tutorial: Time-domain thermoreflectance (TDTR) for thermal property characterization of bulk and thin film materials,” *J. Appl. Phys.*, vol. 124, no. 16, p. 161103, Oct. 2018, doi: 10.1063/1.5046944.
[58] K. B. Myers, P. R. Gaddam, X. Ding, V. Kochergin, S. T. Huxtable, and H. D. Robinson, “Measuring Thermal Conductivity with Magnitude-Dependent Frequency–Domain Thermoreflectance Using Modulated CW Lasers,” *Int. J. Thermophys.*, vol. 39, no. 12, p. 139, Oct. 2018, doi: 10.1007/s10765-018-2458-0.
[59] A. Fleming, C. Folsom, C. Jensen, and H. Ban, “Fiber-based modulated optical reflectance configuration allowing for offset pump and probe beams,” *Rev. Sci. Instrum.*, vol. 87, no. 12, p. 124902, Dec. 2016, doi: 10.1063/1.4967469.
[60] A. Fleming, C. Folsom, C. Jensen, and H. Ban, “Thermal property probe,” US20180156674A1, Jun. 07, 2018.
[61] A. Mandelis, *Diffusion-Waves Fields Mathematical Methods and Green Functions*, 1st ed. New York: Springer, 2001.
[62] C. B. Saltonstall *et al.*, “Complexion dictated thermal resistance with interface density in reactive metal multilayers,” *Phys. Rev. B*, vol. 101, no. 24, p. 245422, Jun. 2020, doi: 10.1103/PhysRevB.101.245422.
[63] Z. Hua, H. Ban, M. Khafizov, R. Schley, R. Kennedy, and D. H. Hurley, “Spatially localized measurement of thermal conductivity using a hybrid photothermal technique,” *J. Appl. Phys.*, vol. 111, no. 10, p. 103505, 2012.
[64] A. Salazar, R. Fuente, E. Apiñaniz, A. Mendioroz, and R. Celorrio, “Simultaneous measurement of thermal diffusivity and optical absorption coefficient using photothermal radiometry. II Multilayered solids,” *J. Appl. Phys.*, vol. 110, no. 3, p. 033516, Aug. 2011, doi: 10.1063/1.3614525.
[65] J. Ordonez-Miranda and J. J. Alvarado-Gil, “Thermal quadrupole method applied to flat and spherical semi-transparent multilayers heated up with a modulated laser beam,” *J. Appl. Phys.*, vol. 112, no. 11, p. 114902, Dec. 2012, doi: 10.1063/1.4767917.

[66] D. M. Camarano, F. A. Mansur, A. M. M. Santos, L. S. Ribeiro, and A. Santos, “Thermal Conductivity of UO2–BeO–Gd2O3 Nuclear Fuel Pellets,” *Int. J. Thermophys.*, vol. 40, no. 12, p. 110, Nov. 2019, doi: 10.1007/s10765-019-2574-5.
[67] J.-C. Krapez and E. Dohou, “Thermal quadrupole approaches applied to improve heat transfer computations in multilayered materials with internal heat sources,” *Int. J. Therm. Sci.*, vol. 81, pp. 38–51, Jul. 2014, doi: 10.1016/j.ijthermalsci.2014.02.007.
[68] K. Alaili, J. Ordonez-Miranda, and Y. Ezzahri, “Modulated heat conduction in a two-layer dielectric system with dynamical interface thermal resistance,” *J. Appl. Phys.*, vol. 124, no. 24, p. 245101, Dec. 2018, doi: 10.1063/1.5058747.
[69] D. Maillet, *Thermal quadrupoles: solving the heat equation through integral transforms*. John Wiley & Sons Inc, 2000.
[70] C. Xing *et al.*, “Parametric study of the frequency-domain thermoreflectance technique,” *J. Appl. Phys.*, vol. 112, no. 10, p. 103105, Nov. 2012, doi: 10.1063/1.4761977.
[71] D. P. Almond and P. M. Patel, *Photothermal Science and Techniques*. Springer Netherlands, 1996.
[72] T. Tomimura, “Experimental Study of Filler Insertion Effect on Mean Thermal Contact Conductance,” *JSME Int. J. Ser. B Fluids Therm. Eng.*, vol. 47, no. 3, pp. 447–452, 2004, doi: 10.1299/jsmeb.47.447.